Applied Catalysis B: Environmental 252 (2019) 47–54

Contents lists available at ScienceDirect

Applied Catalysis B: Environmental

journal homepage: www.elsevier.com/locate/apcatb

In-situ growth of Ag_3PO_4 on calcined Zn-Al layered double hydroxides for enhanced photocatalytic degradation of tetracycline under simulated solar light irradiation and toxicity assessment

Chaorong Chen, Hongyan Zeng*, Moyu Yi, Gaofei Xiao, Sheng Xu*, Shigen Shen, Bo Feng

College of Chemical Engineering, Xiangtan University, Xiangtan, Hunan, 411105, China

ARTICLE INFO

Keywords:
Hydrotalcite
Ag_3PO_4
Photocatalytic degradation
Toxicity assessment

ABSTRACT

The photocatalytic performance of Ag_3PO_4 is severely restricted by the photocorrosion and high charge carrier recombination rate. In order to overcome these defects, a novel Ag_3PO_4/calcined Zn-Al layered double hydroxides (APMO) heterostructure photocatalyst was fabricated via in-situ growth of Ag_3PO_4 particles on the surface of calcined Zn-Al layered double hydroxides (MMO). The crystal structures, morphologies, optical and photoelectrochemical properties of the as-synthesized samples were characterized using various techniques, and its photocatalytic activity for tetracycline (TC) degradation was evaluated under simulated solar light irradiation. Obviously, all the APMO composites demonstrated much higher photocatalytic performances for TC degradation than pure Ag_3PO_4. Especially, the APMO70 showed the highest photocatalytic activity, which was almost about 49.3 times as high as that of pure Ag_3PO_4, and the degradation efficiency was still above 89% after 5 cycles. The improved photocatalytic performance and stability of APMO were ascribed to the efficient charge transfer and strong interfacial contact between Ag_3PO_4 and MMO. The possible photocatalytic mechanisms involving the charge transfer pathway and reactive species generation during the process of TC degradation were also discussed. Finally, the aquatic toxicity of TC was assessed using *Chlorella vulgaris* (*C. vulgaris*) as an ecological indicator, and the result suggested that the as-prepared APMO composite can effectively diminish the aquatic toxicity of TC.

1. Introduction

In the context of energy shortage, the photocatalysis is considered as a great potentiality technology that can utilize solar energy to solve the environment problems [1–10]. In recent years, various semiconductor-based photocatalysts are developed for degradation of organic pollutants in wastewater [11–17]. Due to the high quantum yield and strong oxidative capacity under visible light irradiation, Ag_3PO_4 has been regarded as an effective photocatalyst for organic pollutants degradation [18]. Nevertheless, there are three drawbacks severely restricted its application: (i) the Ag^+ in Ag_3PO_4 is easily reduced to metallic silver (Ag^0) by photogenerated electrons [19]; (ii) the recombination rate of photogenerated election-hole pairs is relatively higher [20]; (iii) the large particle size of Ag_3PO_4 limits the photocatalytic performance [21]. Therefore, numerous studies have devoted to improve the above problems by combining with other semiconductor materials (e.g., g-C_3N_4, $BiVO_4$, and GO) [22–24]. Although the photocatalytic performances of Ag_3PO_4 are improved in this way, a stable and large contact area of Ag_3PO_4-based heterojunction photocatalyst is still of great desired.

Recently, two-dimensional (2D) layer materials have attracted quite a lot of attention on photocatalytic field due to the outstanding performances in electron transport and catalyst supports [25–28]. In all of these, layered double hydroxide (LDH) has been widely used in energy, photocatalytic and environmental pollution control and remediation [29–31]. Especially from the studies of our group and other recent researches, the calcined Zn-Al layered double hydroxides (MMO) can be a potential carrier and/or catalyst for the photocatalytic reaction [9,27,32]. Significantly, the MMO with unique properties is perceived as a very promising candidate in the photocatalytic application because of the following reasons: (i) the higher specific surface area is conducive to the immobilization of catalytically active species and adsorption of pollutants [33]; (ii) the unsaturated metals in the MMO can transfer electrons effectively [34]. In consideration of the excellent properties mentioned above, we expected that the combination of Ag_3PO_4 and MMO should be an effective strategy to form stable heterostructure and

* Corresponding Authors.
E-mail addresses: hyzeng@xtu.edu.cn (H. Zeng), xusheng2016@xtu.edu.cn (S. Xu).

https://doi.org/10.1016/j.apcatb.2019.03.083
Received 16 February 2019; Received in revised form 21 March 2019; Accepted 31 March 2019
Available online 02 April 2019
0926-3373/

protect Ag_3PO_4 from photocorrosion, thus improve the stability, charge separation and interfacial charge transfer efficiency of Ag_3PO_4. Furthermore, the superior surface properties of the MMO also provided an excellent platform for the fabrication of Ag_3PO_4-based heterostructure.

Consequently, we have successfully prepared a novel stable APMO photocatalyst by in situ deposition method in this work. The morphological features, crystal and chemical structures of the as-prepared photocatalysts were characterized in detail and the photocatalytic performances were investigated using tetracycline (TC) as model pollutant under simulated solar light irradiation. Compared with the pure Ag_3PO_4, the APMO photocatalysts showed higher photocatalytic activity. At the same time, the possible mechanisms of inhibition photocorrosion and enhanced photocatalytic activity were proposed investigated. Furthermore, the aquatic toxicity of TC solution at different photocatalytic degradation time was further evaluated using *Chlorella vulgaris* (*C. vulgaris*) as a biological probe.

2. Experiments

2.1. Materials

Sodium phosphate dodecahydrate (Na_3PO_4) were from Shanghai Sinopharm Chemical Reagent Co. Ltd, China, Silver nitrate ($AgNO_3$), zinc nitrate ($Zn(NO_3)_2{\cdot}6H_2O$), aluminum nitrate ($Al(NO_3)_3{\cdot}9H_2O$), urea (CH_4N_2O), sodium hydroxide (NaOH), and hydrochloric acid (HCl) were purchased from Tianjin Damao Chemical Reagent Factory, China. 5,5-dimethyl-pyrroline-N-oxide (DMPO) was purchased from Aladdin Chemical Co., Ltd. Tetracycline (TC) was purchased from Shanghai Shunbo Biological Engineering Co., Ltd, China. All the chemical reagents were analytical grade and used without further purification.

The *C. vulgaris* was purchased from the Freshwater Algae Culture Collection of the Institute of Hydrobiology of Chinese Academy of Sciences, and cultured in OECD medium at 25 ± 0.5 °C under fluorescent lights at 30 μmol photons·m^{-2}·s^{-1} (with light/dark cycle of 12/12 h) according to the organization for economic co-operation and development guideline. During the cultivating of C. vulgaris, every erlenmeyer flask was shaken 3 times a day to avoid the agglomeration of *C. vulgaris* cells. Subsequently, the *C. vulgaris* cells cultured on the 4th day were centrifuged and used for the aquatic toxicity test of TC solution.

2.2. Synthesis of MMO

Zn-Al layered double hydroxides (LDH) were prepared through urea method [35]. Typically, 2.68 *g* $Zn(NO_3)_2{\cdot}6H_2O$, 1.13 *g* $Al(NO_3)_3{\cdot}9H_2O$ and 4.86 *g* urea were dissolved in 150 mL deionized water. After ultrasonic for 30 min, the mixed solution were transferred to three-necked flask and heated at 105 °C for 24 h under vigorous stirring. The suspensions were centrifuged, washed thoroughly by the deionized water and ethanol, and then dried at 60 °C overnight. The MMO powder was obtained from LDH by calcining at 500 °C for 4 h.

2.3. Synthesis of APMO composites

APMO composites were prepared by in situ precipitation method. Firstly, 1.0 *g* MMO powder and an appropriate amount of $AgNO_3$ (0.157 *g*, 0.472 *g*, 0.787 *g*, 1.102 *g*, or 1.417 *g*) were mixed in 150 mL deionized water, and vigorous stirred for 2 h. Subsequently, 150 mL of Na_3PO_4 solution with certain concentration (molar ratio of Ag^+ to PO_4^{3-} is 3.0) was added dropwise into the mixture and kept stirring for 12 h. The final product was collected by centrifugation and washed several times with deionized water and ethanol. After being dried, the obtained product was grounded to powder for further use. According to the mass ratio of Ag^+ to MMO, the as-prepared sample was labeled as APMO10, APMO30, APMO50, APMO70, and APMO90, respectively. For comparison, pure Ag_3PO_4 were also prepared under the same conditions in the absence of MMO.

2.4. Characterization

Powder X-ray diffraction (XRD) measurements were performed on a Japan Rigaku D/max 2550PC (λ = 1.5405 Å) with Cu Kα irradiation. The scan step was 0.02 (2*θ*) with a filament intensity of 30 mA and a voltage of 40 kV. Scanning electron microscopy (SEM, JEOL JSM-6700 F) and transmission electron microscopy (TEM, FEI Talos F200S) were used to observe the morphologies and microstructure of the samples. X-ray photoelectron spectroscopy (XPS) analyses were carried out using a Thermo Fisher Scientific K-Alpha spectrometer. The C1 s peak from the adventitious carbon based contaminant with a binding energy of 284.8 eV was used as the reference for calibration. UV–vis diffuse reflectance spectra (UV–vis DRS) were measured by using a UV–vis spectrophotometer (Shimadzu UV-2550, Kyoto, Japan). The analysis of photoluminescence (PL) spectra was recorded on a fluorescence spectrophotometer (F-4600, Hitachi, Japan) at room temperature. The scanning speed was 1200 nm/min and the width of the emission slit was 5.0 nm. Electrochemical impedance spectroscopy (EIS), transient photocurrent (TPC) response and Mott-Schottky plots were implemented on a CHI 660E workstation in a standard three-electrode system at room temperature. The electrolyte was 0.5 mol·L^{-1} Na_2SO_4 solution, and a 500 W Xe lamp was used as the light source. During the test, the working electrodes were prepared by coating the MMO, Ag_3PO_4, and APMO70 samples on indium-doped tin oxide (ITO) conductive glass, and then immersed into electrolyte. The electron spin resonance (ESR) spectra were recorded on an electron paramagnetic resonance spectrometer (Bruker, A300).

2.5. Photocatalytic experiments and toxicity assays

The photocatalytic degradation TC performances of the as-prepared photocatalysts were tested using a 500 W Xe lamp as simulated solar light irradiation. The temperature of reaction solution was maintained by circulating water jacket. Typically, 50 mg photocatalyst was added into 50 mL TC solution (40 mg L^{-1}). Before irradiation, the mixed solution was vigorously stirred for 30 min to reach adsorption-desorption equilibrium. During the photocatalytic process, 2 mL of the suspension was withdrawn and filtered immediately with 0.22 μm membrane filter at given time intervals. Subsequently, the TC concentration was determined by UV–vis spectrophotometer (752 N spectrophotometer, Shanghai Spectrum Instruments Co., Ltd., China) at 356 nm.

The aquatic toxicity changes of TC solution were assessed by *C. vulgaris*. The prepared *C. vulgaris* cells with initial cell density of 1×10^6 cell·mL^{-1} were transferred to test solutions. The sterilized ultrapure water without TC was used as the medium in the control group, where the TC solutions before and after treated by photocatalysis at different time were used for the test groups. The cell density of *C. vulgaris* was measured every day with UV–vis spectrophotometer at 680 nm.

3. Results and discussion

3.1. Structural characterization

The crystal structure of the LDH, MMO, Ag_3PO_4, and APMO composites were investigated by XRD (Fig. 1). The XRD pattern of LDH showed the characteristic diffraction peaks at 11.7°, 23.6°, 34.6°, 60.2°, and 62.1° corresponds to (003), (006), (009), (110), and (113) planes, which are in agreement with the typical structure of the CO_3^{2-}-intercalated Zn-Al layered double hydroxides [36]. The two peaks at 31.7 and 34.4° observed in MMO are well consistent with the hexagonal wurtzite phase of ZnO [37]. No diffraction peaks of aluminum species were detected in the XRD results, indicating the formation of amorphous aluminum [38]. For the pure Ag_3PO_4, diffraction peaks at 20.9°,

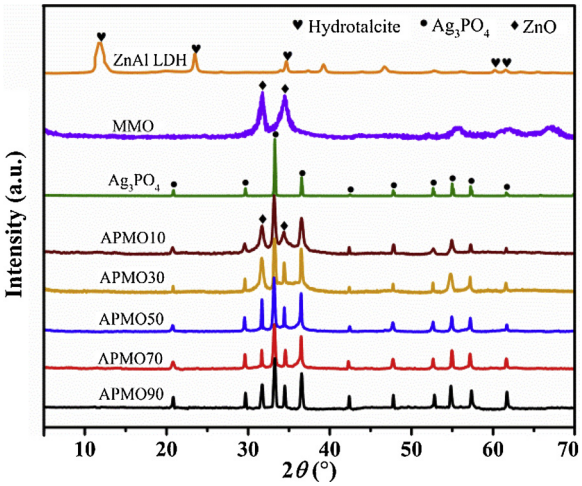

Fig. 1. XRD patterns of the as-prepared samples.

29.7°, 33.3°, 36.6°, 47.8°, 52.7°, 55.0°, 57.2°, 61.6°, and 71.8° were assigned to (110), (200), (210), (211), (310), (222), (320), (321), (400) and (421) planes, which can be indexed to the body-centered cubic structure of Ag_3PO_4 [39,40]. With in situ growth of Ag_3PO_4 on the surface of MMO, the corresponding diffraction peaks of Ag_3PO_4 and MMO can be found in the APMO composites. The results indicated that the combination of Ag_3PO_4 with MMO without affecting the crystal structure of Ag_3PO_4.

The morphologies of pure Ag_3PO_4, MMO, and APMO70 composite were examined by SEM. As seen in Fig. 2a and b, the pure Ag_3PO_4 showed a size of 1.5~2.5 μm regular spheres with smooth surface, while the MMO is composed of some irregularly shaped nanosheets. In comparison with MMO, the APMO70 (Fig. 2c) showed a rough surface decorated with numerous Ag_3PO_4 nanoparticles, and the size of Ag_3PO_4 nanoparticles is much smaller than pure Ag_3PO_4. The corresponding elemental mapping analysis of APMO70 (Fig. 2d) demonstrated the homogeneously distribution of Ag_3PO_4 nanoparticles on the surface of MMO. Further information about the morphology and microstructure of the APMO70 sample were investigated by TEM and HRTEM (Fig. 2e and f). The Ag_3PO_4 nanoparticles with the range of 20~50 nm in size are uniformly deposited on the surface of the MMO. Comparing with the pure Ag_3PO_4, the much smaller Ag_3PO_4 nanoparticles were due to the net trap confinement effect of MMO. The HRTEM images clearly showed the interplanar spacing of 0.268 nm and 0.281 nm, which can be corresponded to the (210) planes of cubic Ag_3PO_4 and (100) planes of ZnO, respectively [39,41].

The bonding configuration of APMO70 was also investigated by XPS. As shown in Fig. 3a, all signals of C, O, Ag, P, Zn and Al were detected and no other impurities were presented in the sample. The two peaks at 367.59 and 373.68 eV in the Ag 3d spectrum (Fig. 3b) can be ascribed to binding energies of Ag $3d_{5/2}$ and Ag $3d_{3/2}$, demonstrating that the silver species existed in the form of Ag^+ in the composite [42]. At the same time, Fig. 3c showed the peak at 132.80 eV is assigned to the P^{+5} in Ag_3PO_4, which is consistent with that reported in literature [20]. For the O 1 s spectrum (Fig. S1), it can be fitted into three peaks. The peak at 530.30 eV is attributed to P = O bond [44], the peak at 531.40 eV ascribed to Zn-O or Al-O bond [45], and the peak at 533.00 eV agreed well with P-O-Ag bond [43].

The optical absorption properties of pure Ag_3PO_4 and APMO composites were investigated by UV–vis DRS (Fig. 4a). The pure Ag_3PO_4 exhibited a broad absorption in the visible region with an absorption edge at about 530 nm. The strong absorption signals in the region of ultraviolet light observed from the APMO composites were contributed to the band-band transition of ZnO [46]. The visible light absorption intensity of the APMO composites were increased obviously, suggesting that loaded Ag_3PO_4 on the surface of MMO is an effective way to improve the light absorption capacity and thus enhance the utilization of solar energy. This phenomenon was also observed in other Ag_3PO_4-based photocatalyst [47]. Subsequently, the PL emission spectrum was applied to investigate the separation efficiency of charge carriers in photocatalysts [48]. Fig. 4b showed the PL spectra of the pure Ag_3PO_4 and APMO composites. Pure Ag_3PO_4 exhibits a strong emission peak at around 530 nm due to the high recombination rate of photogenerated charge carriers, which is consistent with the previous results by Zhang et al [13]. After anchoring Ag_3PO_4 on the surface of MMO, the PL intensity of the APMO composites was weakened significantly,

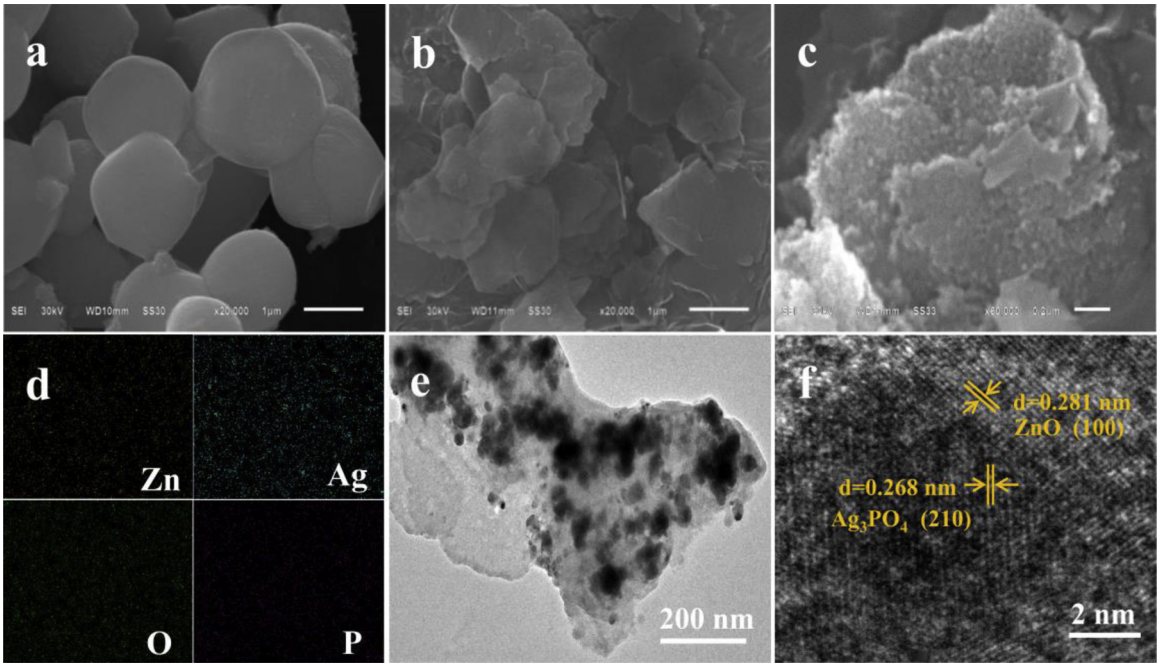

Fig. 2. SEM images of Ag_3PO_4 (a), MMO (b) and APMO70 (c); Corresponding elemental mapping images (d) of Zn, Ag, O, P element in APMO70; TEM (e) and HRTEM (f) image of APMO70.

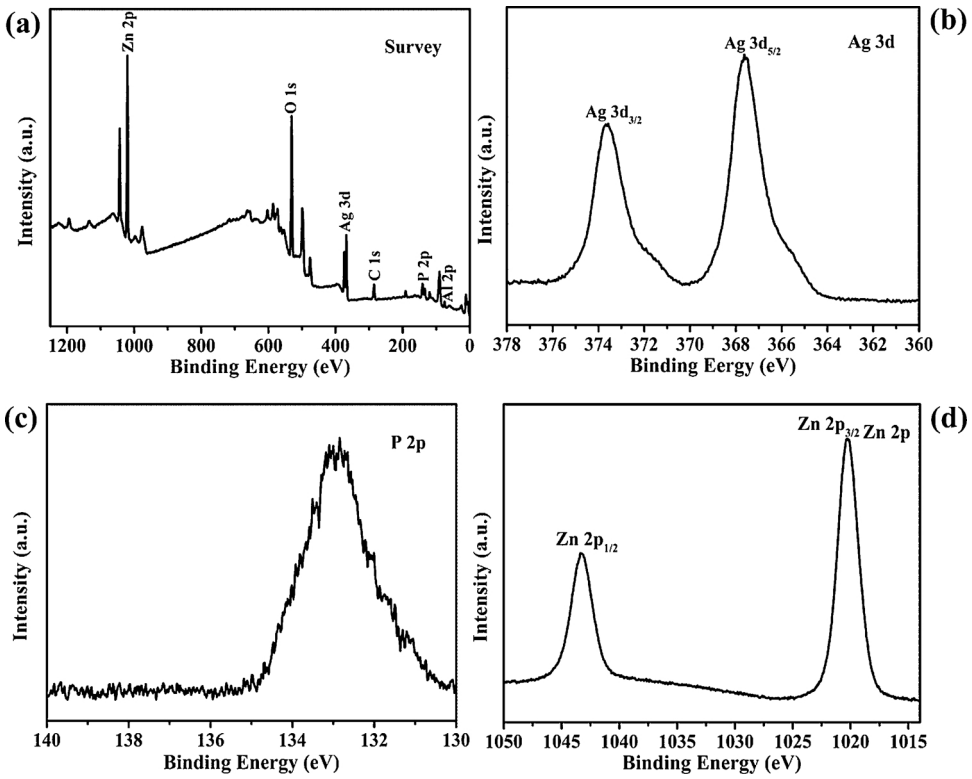

Fig. 3. XPS spectra of APMO70 sample: Survey (a), Ag 3d (b), P 3p (c) and Zn 2p (d).

demonstrating that the formation of heterojunction between Ag_3PO_4 and MMO can effectively promote the separation and transfer of photogenerated charge carriers. In all of the samples, APMO70 showed the lowest PL intensity, which means moderate amount of Ag_3PO_4 was favorable for the separation of charge carriers.

The photoelectrochemical properties of pure Ag_3PO_4, MMO, and APMO70 were investigated to study the separation and transfer efficiency of photogenerated electron-hole pairs. For the electrochemical impedance spectroscopy (EIS) plot, the semicircle part represented the charge transfer-limited process, and the smaller arc of the EIS plot, the smaller charge transfer resistance on the electrode surface [49]. Fig. 5a showed that APMO70 had a smaller arc radius than that of both Ag_3PO_4 and MMO, which demonstrated that the combination of Ag_3PO_4 and MMO can effectively accelerate the separation and transfer of photogenerated electron-hole pairs for APMO70 electrode. In addition, the transient photocurrent (TPC) response of the samples was measured to further confirm the improved charge carriers separation efficiency in APMO70, and the results were presented in Fig. 5b. The TPC curves showed a quick photocurrent response for three samples with the light switch on and off, while the generated photocurrent intensity is rather different. Upon light irradiation, the generated photocurrent of APMO70 electrode (0.076 μA) was about 2.4 and 14.6 times higher than that of Ag_3PO_4 and MMO electrode, respectively. The results further revealed that the formation of Ag_3PO_4/MMO composite can efficiently enhance the transfer and separation of photogenerated electron-hole pairs.

The flat band potentials (E_{fb}) of Ag_3PO_4 and MMO were estimated by Mott-Schottky measurement. As shown in Fig. S2, both of Ag_3PO_4 and MMO presented a positive slope in Mott-Schottky plots, suggesting that they are n-type semiconductors. The E_{fb} of Ag_3PO_4 and MMO can be obtained by extrapolating the linear region of the curve to $1/C^2 = 0$. In general, the conduction band (CB) potential of n-type semiconductor is nearly equal to the E_{fb} [50]. Thus, the CB of Ag_3PO_4 and MMO were estimated to be 0.22 and −0.78 V vs. Ag/AgCl (equivalent to 0.44 V and −0.58 V vs. NHE), respectively.

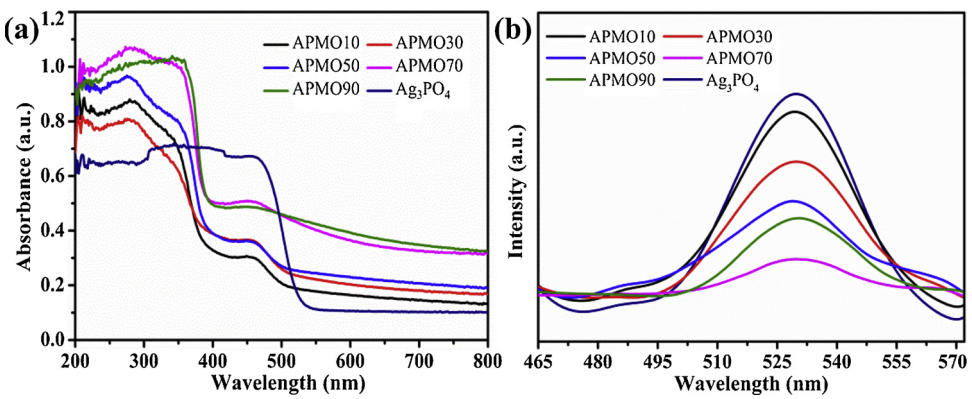

Fig. 4. UV–vis DRS (a) and PL (b) spectra of Ag_3PO_4 and APMO composite with various Ag contents.

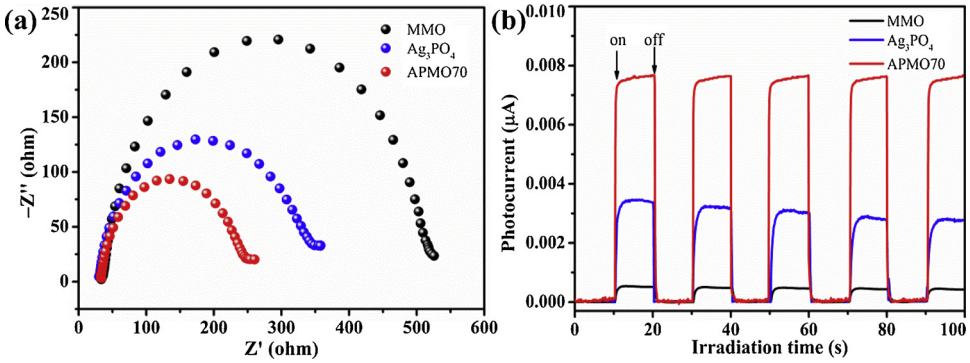

Fig. 5. EIS Nyquist plots (a) and TPC responses (b) of Ag_3PO_4, MMO and APMO70.

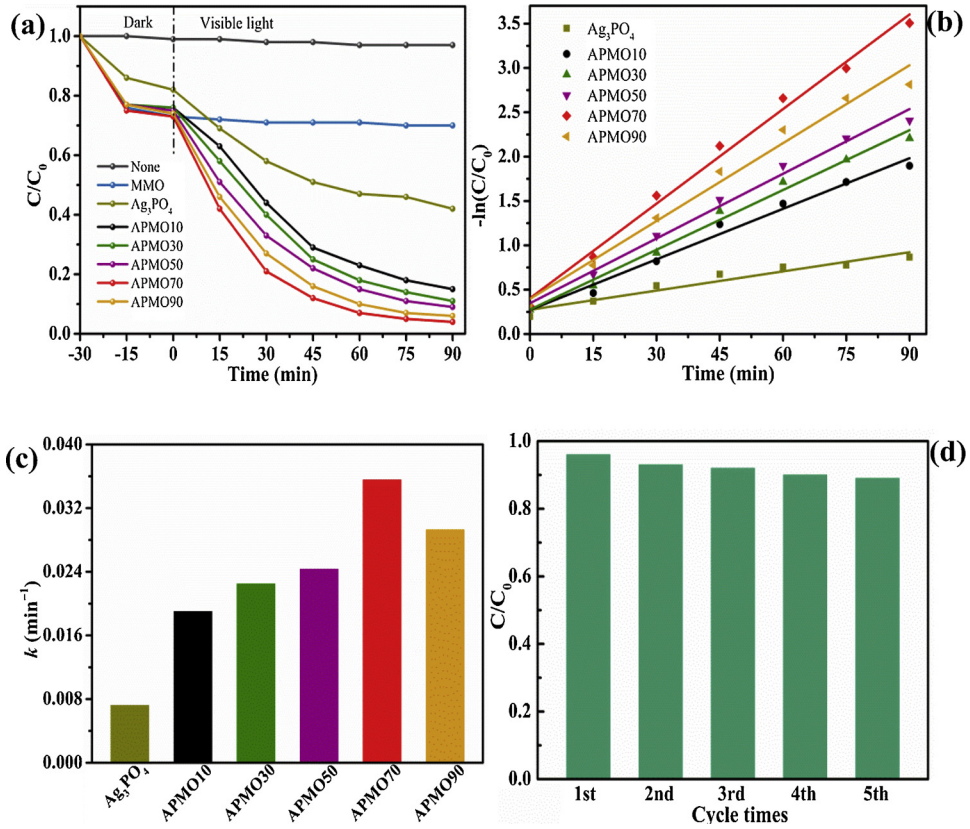

Fig. 6. Photocatalytic degradation of TC by as-prepared samples under simulated solar light: degradation efficiency (a), pseudo-first order kinetics (b), the apparent reaction rate constants (c); recycling runs over APMO70 for TC degradation under simulated solar light (d).

3.2. Photocatalytic efficiency

In order to evaluate the photocatalytic activity of pure Ag_3PO_4, MMO and APMO composites, TC was chosen as model pollutant for the photocatalytic reaction under simulated solar light irradiation. As shown in Fig. 6a, the blank test indicated that the degradation of TC can be ignored in the absence of the photocatalyst. The MMO exhibited 27% TC adsorption efficiency in the dark and negligible photocatalytic activity. It is found that the APMO composites possessed higher adsorption capacity than pure Ag_3PO_4 owing to the abundant adsorption sites on the surface of MMO. The TC degradation efficiency of APMO composites increased firstly with the Ag^+ content from 10% to 70% and then decreased by increasing the Ag^+ content to 90%. The APMO70 photocatalyst achieved the highest photocatalytic activity, the degradation efficiency of TC reached 96% within 90 min. The decreased photocatalytic activity of APMO90 could be related to the excessive Ag_3PO_4 aggregated on the surface of MMO, which resulted in reducing of efficient heterojunctions. Furthermore, the degradation kinetics of TC was studied using the pseudo-first-order model ($-\ln(C/C_0) = kt$) [1]. As seen in Fig. 6b, the photocatalytic reaction time t (min) is close to the straight line with $-\ln(C/C_0)$, demonstrating that the TC degradation process is fitted well with pseudo-first-order kinetics. The corresponding apparent reaction rate (k) were calculated and presented in Fig. 6c, the APMO70 had the highest k value (0.3555 min^{-1}), which was about 49.3 times high than that of pure Ag_3PO_4 (0.0072 min^{-1}). Besides, the reusability testing of APMO70 was conducted for 5 cycles. After each cycle, the photocatalyst was collected by centrifuging, washing and drying, and then used for the next run. As shown in Fig. 6d, the degradation efficiency of TC showed no obvious loss and still remained about 89% after being used for 5 cycles. To further verify the good structural stability of APMO70, the Ag 3d XPS spectra of APMO70 after photocatalytic degradation of TC was measured. The two peaks of Ag $3d_{3/2}$ and $3d_{5/2}$ in Fig. S3 showed no obvious changes, indicating that the silver species in the composite after 5 cycles are still

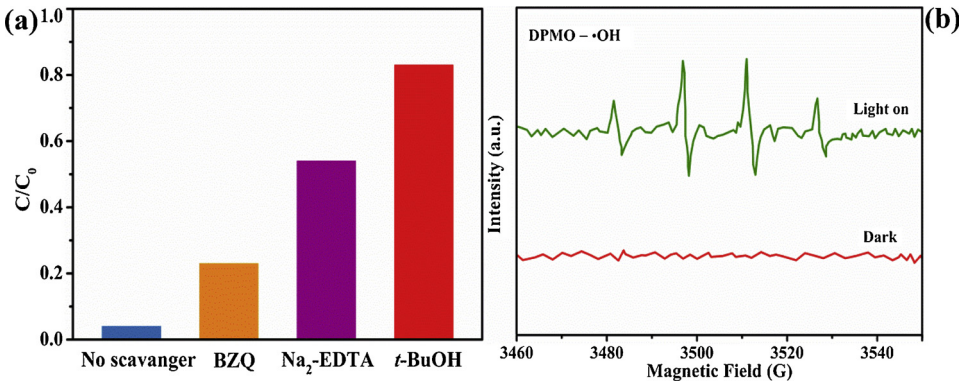

Fig. 7. Trapping experiment of the active species over APMO70 for TC degradation (a) and ESR spectra of DMPO-•OH in aqueous dispersions recorded with APMO70 under simulated solar light irradiation (b).

existed in the form of Ag^+. The results demonstrated that the APMO70 photocatalyst possessed excellent photocatalytic stability.

3.3. Possible photocatalytic mechanism

In order to identify the contribution degree of active species in the TC degradation process, radicals and holes trapping experiments were conducted. In this study, disodium ethylenediaminetetraacetate (EDTA-Na_2), benzoquinone (BZQ), and tert-butanol (*t*-BuOH) were used as the scavenger of hole (h^+), superoxide radical ($\bullet O_2^-$), and hydroxyl radical (•OH), respectively [51,52]. The dosages of all scavengers are 1 mM. As shown in Fig. 7a, the photocatalytic efficiency of the APMO70 declined significantly from 96% to 17% after the addition of *t*-BuOH, indicating that •OH played a major role in photocatalytic degradation of TC. The degradation efficiency decreased to 46% with the addition of h^+ scavenger EDTA-Na_2, which verified that the h^+ also has positive effects on the reaction. In addition, the addition of BZQ resulted in a slight decrease in degradation efficiency from 96% to 77%, indicating that $\bullet O_2^-$ was not the main reactive species during the TC degradation process. According to the experimental results achieved above, •OH and h^+ are the predominant active species in TC degradation reaction. In addition, the generation of •OH radicals was further verified by ESR technique and the results are shown in Fig. 7b. Four characteristic peaks with an intensity ratio of 1:2:2:1 were observed under simulated solar light irradiation, while no signals were detected in the aqueous dispersion of APMO70 in dark. The ESR results demonstrated that •OH radicals can be produced during the photocatalytic process.

On the basis of the experimental results above, the possible photocatalytic mechanism for TC degradation over the APMO composite has been proposed and illustrated in Scheme 1. The bandgap energy of Ag_3PO_4 and MMO were determined from the plots of $(ahv)^2$ against (hv) (Fig. S4), corresponding to a band gap energy of 2.45 and 3.12 eV, respectively. When the simulated solar light irradiated, both Ag_3PO_4 and MMO can be excited and formed photogenerated electron-hole pairs. The excited electrons (e^-) on the conduction band (CB) of MMO (-0.58 eV) can be directly immigrated onto the CB of Ag_3PO_4 (+ 0.44 eV) due to the more negative CB position of MMO, thus promoted the separation of photogenerated electron-hole pairs. Then, the injected e^- on the CB of Ag_3PO_4 can reduce the adsorbed O_2 to H_2O_2, because of the more negative position than O_2/H_2O_2 potential (+0.68 V vs NHE) [53], and the produced H_2O_2 can further react with e^- to produce •OH. The generation of H_2O_2 during photocatalytic reaction was verified by triiodide method (Fig. S5) [54]. As the CB of Ag_3PO_4 is more positive than $O_2/\bullet O_2^-$ potential (-0.046 V vs NHE) [55], the accumulated electrons on the CB of Ag_3PO_4 cannot reduce O_2 to produce $\bullet O_2^-$. Simultaneously, the holes (h^+), transferred from the valence band (VB) of Ag_3PO_4 (+ 2.89 eV) to the VB of MMO (+ 2.54 eV), can react with OH^- to produce •OH due to the more positive VB position than OH^-/•OH potential (+1.99 V vs NHE) [55]. Subsequently, the generated •OH and h^+ as the main active species are participated in the reaction of TC degradation, which is in agreement with the analysis of reactive species above.

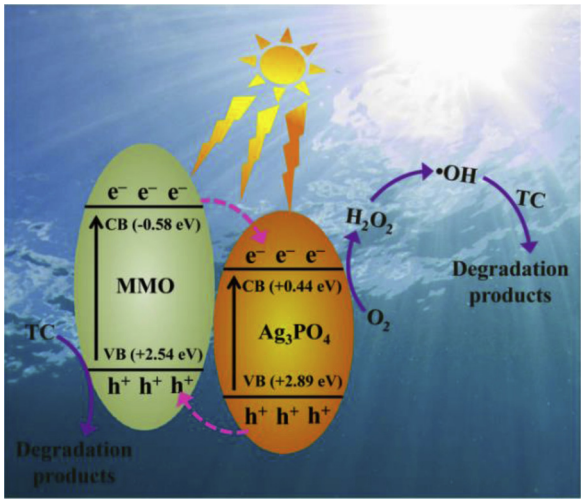

Scheme 1. Possible photocatalytic mechanism for TC degradation and charge transfer process.

3.4. Toxicity assessment

The ultimate goal of degrading contaminants is to decrease the aquatic toxicity. Thus, the aquatic toxicity of TC solution before and after treated by photocatalysis at different time was assessed using *C. vulgaris* as an ecological indicator (Fig. 8). For the control, the cell density of *C. vulgaris* was about 39.2×10^5 cell·mL^{-1} after 4 days of cultivation, while the cell density in the untreated TC solution was decreased on the first day and then increased with a slow rate of growth, and the cell density of *C. vulgaris* was only 8.2×10^5 cell·mL^{-1} in the end. The results indicated that TC had significant inhibitory effects on the growth of *C. vulgaris*. After treated by photocatalytic, the inhibitory effects reduced gradually, the cell density of *C. vulgaris* in the 90 min-photocatalytic treated TC solution showed the highest cell density (41.1×10^5 cell·mL^{-1}). For further comparison, the inhibitory rate on the 4th day was calculated according to the literature [56]. The untreated TC solution showed the highest inhibitory rate (79.2%), and then gradually decreased with increasing irradiation time (39.4, 15.1, 10.0, and -5.0%), implying that the TC molecules were degraded into less dangerous forms during the photocatalytic degradation process. The toxicity of 90 min-photocatalytic treated TC solution almost vanished and showed a stimulatory effect on the growth of *C. vulgaris*,

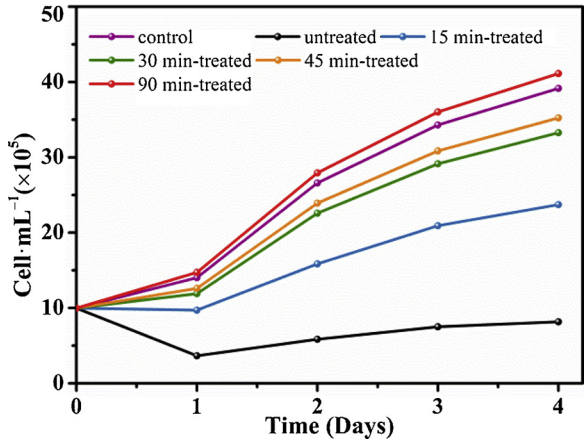

Fig. 8. Growth of *C. vulgaris* exposed to TC solution collected at different photocatalytic degradation time.

which could be related to the presence of some beneficial degradation products [57] and/or hormesis phenomenon [58]. The results suggested that the aquatic toxicity of TC can be efficiently reduced by the photocatalytic degradation progress in APMO70 system under simulated solar light irradiation.

4. Conclusions

In this study, novel APMO heterostructure photocatalysts with different Ag^+ content were successfully prepared via in-situ precipitation method. The results indicated that the combination of Ag_3PO_4 and MMO can significantly enhance the photocatalytic activity for TC degradation, and the photocatalytic performance of APMO composite was depended on the content of Ag^+. The APMO70 showed the highest photocatalytic performance under simulated solar light irradiation, and the *k* value was nearly 49.3 times higher than that of Ag_3PO_4. The excellent photocatalytic performances of APMO composites were mainly derived from the improved separation and transfer efficiency of photogenerated charge carriers. The well-matched band structure between Ag_3PO_4 and MMO effectively protected Ag_3PO_4 from photocorrosion, and resulted in a high photocatalytic stability of APMO composites. The trapping experiments showed that •OH and h^+ are the mainly active species in the photocatalytic reaction process. Moreover, the results of toxicity assessment suggested that APMO can be an effective photocatalyst for degrading and reducing the aquatic toxicity of TC.

Acknowledgments

This work was supported by the National Natural Science Foundation of China (No. 21777135), Key Research and Development Program of Hunan Province (2018SK20110), Hunan Provincial Innovation Foundation for Postgraduate (CX2018B043), Xiangtan University undergraduate innovative experiment program (2018XTUXJ036) and Xiangtan University Undergraduate Innovative Experiment Program (2018XTUXJ036) and Hunan 2011 Collaborative Innovation Center of Chemical Engineering & Technology with Environmental Benignity.

Appendix A. Supplementary data

Supplementary material related to this article can be found, in the online version, at doi:https://doi.org/10.1016/j.apcatb.2019.03.083.

References

[1] Y. Liu, G. Zhu, J. Gao, M. Hojamberdiev, R. Zhu, X. Wei, Q. Guo, P. Liu, Appl. Catal. B Environ. 200 (2017) 72–82.
[2] P. Yao, H. Liu, D. Wang, J. Chen, G. Li, T. An, J. Colloid. Interf. Sci. 522 (2018) 174–182.
[3] L.N. Song, F. Ding, Y.K. Yang, D. Ding, L. Chen, C.T. Au, S.F. Yin, ACS Sustain. Chem. Eng. 6 (2018) 17044–17050.
[4] Y. Yang, C. Zhang, D. Huang, G. Zeng, J. Huang, C. Lai, C. Zhou, W. Wang, H. Guo, W. Xue, R. Deng, M. Cheng, W. Xiong, Appl. Catal. B Environ. 245 (2019) 87–99.
[5] B. Li, C. Lai, G. Zeng, L. Qin, H. Yi, D. Huang, C. Zhou, X. Liu, M. Cheng, P. Xu, C. Zhang, F. Huang, S. Liu, ACS Appl. Mater. Inter. 10 (2018) 18824–18836.
[6] H. Yi, D. Huang, L. Qin, G. Zeng, C. Lai, M. Cheng, S. Ye, B. Song, X. Ren, X. Guo, Appl. Catal. B Environ. 239 (2018) 408–424.
[7] P. Chen, L. Chen, Y. Zeng, F. Ding, X. Jiang, N. Liu, C.T. Au, S.F. Yin, Appl. Catal. B Environ. 234 (2018) 311–317.
[8] J. He, L. Chen, D. Ding, Y.K. Yang, C.T. Au, S.F. Yin, Appl. Catal. B Environ. 233 (2018) 243–249.
[9] C.R. Chen, H.Z. Zeng, S. Xu, J.C. Shen, G. Hu, R.L. Zhu, J.Z. Du, Y.X. Sun, Appl. Clay Sci. 165 (2018) 197–204.
[10] J. Schneider, M. Matsuoka, M. Takeuchi, J. Zhang, Y. Horiuchi, M. Anpo, D.W. Bahnemann, Chem. Rev. 114 (2014) 9919–9986.
[11] Y. Liu, G. Zhu, J.Z. Gao, M. Hojamberdiev, H. Luo, R. Zhu, X. Wei, P. Liu, J. Alloys. Compd. 688 (2016) 487–496.
[12] S. Fan, X. Li, M. Qin, J. Mu, L. Wang, G. Gan, X. Wang, A. Chen, ACS Omega 4 (2019) 4113–4128.
[13] W. Zhang, G. Li, W. Wang, Y. Qin, T. An, X. Xiao, W. Choi, Appl. Catal. B Environ. 232 (2018) 11–18.
[14] M. Wu, H. Lv, T. Wang, Z. Ao, H. Sun, C. Wang, T. An, S. Wang, Catal. Today 315 (2018) 205–212.
[15] J. Sun, X. Li, Q. Zhao, M.O. Tadéc, S. Liu, Appl. Catal. B Environ. 219 (2017) 259–268.
[16] Y. Shi, Z. Yang, B. Wang, H. An, Z. Chen, H. Cui, Appl. Clay Sci. 119 (2016) 311–320.
[17] T. Xu, R. Zhu, J. Zhu, X. Liang, Y. Liu, Y. Xu, H. He, Catal. Sci. Technol. 6 (2016) 4116–4123.
[18] X. Yang, H. Cui, Y. Li, J. Qin, R. Zhang, H. Tang, ACS Catal. 3 (2013) 363–369.
[19] H. Xu, C. Wang, Y. Song, J. Zhu, Y. Xu, J. Yan, Y. Song, H. Li, Chem. Eng. J. 241 (2014) 35–42.
[20] L. Zhou, W. Zhang, L. Chen, H. Deng, J. Colloid. Interf. Sci. 487 (2017) 410–417.
[21] E. Abroshan, S. Farhadi, A. Zabardasti, Sol. Energy Mater. Sol. Cells 178 (2018) 154–163.
[22] H. Katsumata, T. Sakai, T. Suzuki, S. Kaneco, Ind. Eng. Chem. Res. 53 (2014) 8018–8025.
[23] X. Qi, M. Gu, X. Zhu, J. Wu, Q. Wu, H. Long, K. He, Mater. Res. Bull. 80 (2016) 215–222.
[24] Q. Xiang, D. Lang, T. Shen, F. Liu, Appl. Catal. B Environ. 162 (2015) 196–203.
[25] D. Deng, K.S. Novoselov, Q. Fu, N. Zheng, Z. Tian, X. Bao, Nat. Nanotechnol. 11 (2016) 218–230.
[26] J. Zhang, Y. Chen, X. Wang, Synth. Lect. Energy Environ. Technol. Sci. Soc. 8 (2015) 3092–3108.
[27] Y. Cao, G. Li, X. Li, Chem. Eng. J. 292 (2016) 207–223.
[28] H. Yin, Z. Tang, Chem. Soc. Rev. 45 (2016) 4873–4891.
[29] J. Han, Y. Dou, J. Zhao, M. Wei, D.G. Evans, X. Duan, Small 9 (2013) 98–106.
[30] K. Parida, L. Mohapatra, Dalton Trans. 41 (2012) 1173–1178.
[31] M. Xu, B. Bi, B. Xu, Z. Sun, L. Xu, Appl. Clay Sci. 157 (2018) 86–91.
[32] Z. Huang, P. Wu, B. Gong, Y. Fang, N. Zhu, J. Mater. Chem. A 2 (2014) 5534–5540.
[33] S. He, Z. An, M. Wei, D.G. Evans, X. Duan, Chem. Commun. 49 (2013) 5912–5920.
[34] M.J. Wu, J.Z. Wu, J. Zhang, H. Chen, J.Z. Zhou, G.R. Qian, Z.P. Xu, Z. Du, Q.L. Rao, Catal. Sci. Technol. 8 (2018) 1207–1228.
[35] L. Zhang, J. Liu, H. Xiao, D. Liu, Y. Qin, H. Wu, H. Li, N. Du, W. Hou, Chem. Eng. J. 250 (2014) 1–5.
[36] X. Yuan, W. Li, Appl. Clay Sci. 138 (2017) 107–113.
[37] K. Wang, J. Xu, X. Wang, Appl. Surf. Sci. 360 (2016) 270–275.
[38] M. Hu, H. Lou, X. Yan, X. Hu, R. Feng, M. Zhou, Microporous Mesoporous Mater. 271 (2018) 68–72.
[39] L. Liu, Y. Qi, J. Lu, S. Lin, W. An, Y. Liang, W. Cui, Appl. Catal. B Environ. 183 (2016) 133–141.
[40] Y. Bu, Z. Chen, ACS Appl. Mater. Inter. 6 (2014) 17589–17598.
[41] J. Huang, Z. Yang, R. Wang, Z. Zhang, Z. Feng, X. Xie, J. Mater. Chem. A 3 (2015) 7429–7436.
[42] W. Zhao, J. Zhang, J. Pan, W. Zhao, J. Niu, J. Qiu, C. Li, Ceram. Int. 44 (2018) 18337–18343.
[43] R. Liu, H. Li, L. Duan, H. Shen, Q. Zhang, X. Zhao, Appl. Surf. Sci. 462 (2018) 263–269.
[44] P. Dong, G. Hou, C. Liu, X. Zhang, H. Tian, F. Xu, X. Xi, R. Shao, Materials 9 (2016) 968.
[45] J. Rong, H. Chen, F. Qiu, T. Zhang, Y. Zhu, D. Yang, J. Xu, X. Rong, Q. Guo, X. Peng, J. Taiwan Inst. Chem. E. 88 (2018) 78–88.
[46] J.C. Sin, S.M. Lam, K.T. Lee, A.R. Mohamed, Ceram. Int. 40 (2014) 5431–5440.
[47] X. Lin, X. Guo, W. Shi, F. Guo, G. Che, H. Zhai, Y. Yan, Q. Wang, Catal. Commun. 71 (2015) 21–27.
[48] P. Wang, Y. Tang, Z. Dong, Z. Chen, T.T. Lim, J. Mater. Chem. A 1 (2013) 4718–4727.
[49] Y. He, L. Zhang, B. Teng, M. Fan, Environ. Sci. Technol. 49 (2014) 649–656.

[50] T. Xu, R. Zhu, G. Zhu, J. Zhu, X. Liang, Y. Zhu, H. He, Appl. Catal. B Environ. 212 (2017) 50–58.
[51] M. Wu, D. Xu, B. Luo, H. Shen, C. Wang, W. Shi, Mater. Lett. 161 (2015) 45–48.
[52] Y. Yang, Z. Ma, L. Xu, H. Wang, N. Fu, Appl. Surf. Sci. 369 (2016) 576–583.
[53] K. Fuku, Y. Miyase, Y. Miseki, T. Funaki, T. Gunji, K. Sayama, Chem. Asian J. 12 (2017) 1111–1119.
[54] G. Dong, Z. Ai, L. Zhang, RSC Adv. 4 (2014) 5553–5560.
[55] Y. Zhu, R. Zhu, L. Yan, H. Fu, Y. Xi, H. Zhou, G. Zhu, J. Zhu, H. He, Appl. Catal. B Environ. 239 (2018) 280–289.
[56] Y. Qian, X. Li, R. Tian, Ecotox. Environ. Safe. 168 (2019) 401–407.
[57] W. Baran, J. Sochacka, W. Wardas, Chemosphere 65 (2006) 1295–1299.
[58] X.Y. Liu, H.Z. Zeng, M.C. Liao, B. Feng, B.F.C.A. Gohi, Biochem. Eng. J. 97 (2015) 125–131.